Atomic Layer Deposition of Molybdenum and Tungsten Oxide Thin Films Using Heteroleptic Imido-Amidinato Precursors : Process Development, Film Characterization, and Gas Sensing Properties

Mattinen, Miika

2018-12-11

Mattinen , M , Wree , J-L , Stegmann , N , Ciftyurek , E , El Achhab , M , King , P J , Mizohata , K , Räisänen , J , Schierbaum , K D , Devi , A , Ritala , M & Leskelä , M 2018 , ' Atomic Layer Deposition of Molybdenum and Tungsten Oxide Thin Films Using Heteroleptic Imido-Amidinato Precursors : Process Development, Film Characterization, and Gas Sensing Properties ' , Chemistry of Materials , vol. 30 , no. 23 , pp. 8690-8701 . https://doi.org/10.1021/acs.chemmat

http://hdl.handle.net/10138/306899
https://doi.org/10.1021/acs.chemmater.8b04129

acceptedVersion

Atomic Layer Deposition of Molybdenum and Tungsten Oxide Thin Films Using Heteroleptic Imido-Amidinato Precursors: Process Development, Film Characterization, and Gas Sensing Properties

Miika Mattinen,[*†] Jan-Lucas Wree,[‡] Niklas Stegmann,[‡] Engin Ciftyurek,[¥] Mhamed El Achhab,[¥] Peter J. King,[†] Kenichiro Mizohata,[§] Jyrki Räisänen,[§] Klaus D. Schierbaum,[¥] Anjana Devi,[‡] Mikko Ritala,[*†] Markku Leskelä[†]

† Department of Chemistry, University of Helsinki, P.O. Box 55, 00014, Finland

‡ Inorganic Materials Chemistry, Faculty of Chemistry and Biochemistry, Ruhr-University Bochum, Universitätsstr. 150, 44801 Bochum, Germany

¥ Material Science Department, Institute of Experimental Condensed Matter Physics, Heinrich Heine University Düsseldorf, Universitätsstr. 1, 40225, Düsseldorf, Germany

§ Division of Materials Physics, Department of Physics, University of Helsinki, P.O. Box 43, 00014, Finland

ABSTRACT: Heteroleptic bis(tert-butylimido)bis(*N,N'*-diisopropylacetamidinato) compounds of molybdenum and tungsten are introduced as precursors for atomic layer deposition (ALD) of tungsten and molybdenum oxide thin films using ozone as the oxygen source. Both precursors have similar thermal properties, but exhibit different growth behavior. With the molybdenum precursor, high growth rates up to 2 Å/cycle at 300 °C and extremely uniform films are obtained, although the surface reactions are not completely saturative. The corresponding tungsten precursor enables saturative film growth with a lower growth rate of 0.45 Å/cycle at 300 °C. Highly pure films of both metal oxides are deposited and their phase as well as stoichiometry can be tuned by changing the deposition conditions. The WO_x films crystallize as γ-WO_3 at 300 °C and above while the films deposited at lower temperatures are amorphous. Molybdenum oxide can be deposited as either amorphous (≤ 250 °C), crystalline suboxide (275 °C), a mixture of suboxide and α-MoO_3 (300 °C), or pure α-MoO_3 films (≥ 325 °C). MoO_x films are further characterized by synchrotron photoemission spectroscopy and temperature-dependent resistivity measurements. A suboxide MoO_x film deposited at 275 °C is demonstrated to serve as an efficient hydrogen gas sensor at a low operating temperature of 120 °C.

Introduction

Molybdenum and tungsten have versatile yet rather similar oxide chemistry. Both elements form various compounds with different oxidation states, crystalline structures, and physical as well as chemical properties.[1–6] The most important and stable oxides are the trioxides MO_3 (M = Mo, W), which exhibit several polymorphs and are wide band-gap semiconductors (E_g ≈ 2.5–3.5 eV) with poor electrical conductivity in pristine form. In reducing conditions the trioxides easily form oxygen vacancies as well as crystalline suboxide phases, such as Mo_4O_{11} ($MoO_{2.75}$), $Mo_{17}O_{47}$ (≈$MoO_{2.76}$), Mo_8O_{23} (≈$MoO_{2.88}$), and Mo_9O_{26} (≈$MoO_{2.89}$) for molybdenum, and $W_{32}O_{84}$ ($WO_{2.625}$), $W_{18}O_{49}$ (≈$WO_{2.72}$), $W_{17}O_{47}$ (≈$WO_{2.76}$), and $W_{20}O_{58}$ ($WO_{2.9}$) for tungsten.[4–7] The oxygen-deficient forms exhibit increased electrical conductivity and even metallic behavior.[2,7–9] The dioxides MO_2 are well-known metallic conductors.[10]

The similarities of molybdenum and tungsten oxides extend to the studied range of applications of MO_3 and suboxides,[1–3] which include smart windows and other optical coatings,[11] (photo)catalysis,[12–14] gas sensors,[15,16] non-volatile memories,[17–19] and lithium ion batteries.[20] Obviously, as each crystalline phase has a different structure and properties, their performance in different applications vary accordingly.[14,21–24]

To highlight one promising application, MoO_3 has recently been studied as a sensor for gases such as H_2,[25–30] O_2,[31] O_3,[31] NH_3,[30] NO_2,[26,31] and SO_2.[32] Advantageously, MoO_3 sensors may be operated at moderate temperatures, usually from 200 to 400 °C.[25,26,29,30] Hydrogen gas sensors, in particular, are rapidly gaining importance as hydrogen is being increasingly used as a clean energy source. H_2 is a highly flammable yet colorless and odorless gas. Therefore, sensitive, reliable, and fast hydrogen sensors are needed to enable safe storage, transport, and use of hydrogen.[33] Although various nanostructured forms of α-MoO_3 have shown respectable performance in H_2 sensing,[25,27,28] suboxide MoO_x phases have not, to the best of our knowledge, been studied as H_2 sensors.

As outlined above, controlled deposition of uniform thin films and other nanostructures of molybdenum and tungsten oxides with desired phase and morphology is required to achieve optimal performance in different applications. As discussed in detail by de Castro et al.[1] and Zheng et al.[3], MoO_x and WO_x thin films and other nanostructures are typically deposited using techniques such as electrodeposition, hydro- or solvothermal synthesis, sol-gel process, chemical vapor deposition (CVD), and different physical vapor deposition (PVD) methods. However, using these methods, uniform coating on micro- and nanostructured substrates with high surface areas is rarely demonstrated and can be difficult or even impossible to accomplish. On the contrary, using atomic layer deposition (ALD), an advanced gas-phase thin film deposition method based on self-limiting surface reactions of alternately pulsed precursors, uniform coating of both large and complex substrates with accurately controlled film thickness and excellent reproducibility is easily achieved. ALD typically produces high-quality films at relatively low deposition temperatures and is also straightforward to scale up for industrial use.[34–36]

ALD is a chemical technique with several requirements for the precursors,[34] including volatility, thermal stability, high reactivity, and lack of etching or dissolution reactions with the film or substrate. Thus, synthesizing, identifying, and evaluating suitable precursors are key steps in developing ALD processes. Due to the similar chemical properties of molybdenum and tungsten, analogous compounds have often been used as ALD precursors to deposit oxides of both metals, including $[M(CO)_6]$,[37–39] $[M(N^tBu)_2(NMe_2)_2]$,[40–43] and $[MO_2(^tBuamd)_2]$ (M = Mo, W).[44] However, some differences have been reported in the reactivity of the molybdenum and tungsten compounds under ALD conditions. For example, $[W(N^tBu)_2(NMe_2)_2]$ reacts with H_2O,[43] whereas the corresponding Mo compound requires the use of more reactive O_3 or O_2 plasma.[40,41] Additionally, some other metal precursors have been used to deposit either MoO_x[45–49] or WO_x[50–53] by ALD. Nevertheless, ALD of crystalline MoO_x[48] or WO_x[38,51] films without the use of plasma-enhancement or post-deposition annealing has been rarely achieved and only limited control over the different crystalline phases has been demonstrated. Therefore, it is evident that further efforts in precursor development are required to identify precursors that combine adequate thermal stability and reactivity with the ability to control the phase composition of the MoO_x and WO_x films.

In this report, we have studied all-nitrogen coordinated, heteroleptic bis(imido)-bis(amidinato) compounds $[M(N^tBu)_2(dpamd)_2]$ (M = Mo, W; dpamd = diisopropylacetamidinate) as ALD precursors. The compounds have promising thermal properties and have previously been used to deposit WO_xN_y,[54] WO_3,[55] MN_x,[56] and MS_2[57] films by CVD. The suitability of these precursors for ALD of MoO_x and WO_x ($x \approx 3$) is shown using ozone as a reactant. Growth characteristics and film structure are examined in detail for both oxides. Clear differences between the metals are observed in terms of growth rates and crystallization behavior. Temperature-dependent resistivity and hydrogen gas sensing properties of MoO_x films are further evaluated to highlight the high quality and performance of the deposited films.

Experimental section

Molybdenum and tungsten oxide films were deposited in a commercial, hot wall, cross-flow ASM F120 ALD reactor[58] operating at approximately 5 mbar. Nitrogen (N_2, AGA, 99.999%) served both as carrier and purge gas. The films were mostly deposited on 5 × 5 cm^2 silicon (100) and soda lime glass substrates. The glass substrates were cleaned using successive ultrasonic baths of alkaline ultrasonic cleaning solution, tap water, ethanol, and de-ionized water. The silicon substrates were blown clean of particles using pressurized nitrogen. 4 × 4 mm^2 SiO_2(500 nm)/Si substrates fixed to a 5 × 5 cm^2 Si carrier substrate with double-sided Kapton tape were used to prepare samples for the temperature-dependent resistivity and gas sensing measurements.

Bis(tert-butylimido)bis(*N,N'*-diisopropylacetamidinato) compounds of molybdenum and tungsten were synthesized by salt methathesis.[59] The compounds were evaporated from open glass boats inside the ALD reactor heated to 145 °C for $[Mo(N^tBu)_2(dpamd)_2]$ and 155 °C for $[W(N^tBu)_2(dpamd)_2]$. The precursors were delivered to the substrates by N_2 carrier gas flow and the pulsing was achieved by inert gas valving.[58] Thermogravimetric analysis (TGA) of the precursors was performed using a Mettler Toledo STARe system equipped with a TGA850 thermobalance under atmospheric pressure of N_2. The heating rate was 10 °C/min and the sample size was approximately 10 mg.

Ozone (O_3) was produced from oxygen (O_2, AGA, 99.999%) using an ozone generator (Wedeco Ozomatic Modular 4 HC) resulting in an O_3-O_2 mixture with a nominal O_3 concentration of 100 g/Nm^3. The flow rate of the O_3-O_2 mixture was typically set to approximately 200 sccm using a needle valve. Unless otherwise noted, the films were deposited at 300 °C using 1 s metal precursor and 5 s O_3 pulses separated by 1 s N_2 purges.

Further film deposition tests were done using de-ionized H_2O, H_2S (AGA, 99.5%), and NH_3 (AGA, 99.999%) as the reactant. The reactants were pulsed by mechanical solenoid valves with flow rates set to approximately 10 sccm for H_2S and NH_3 during continuous flow using needle valves.

Film thicknesses were primarily measured by a Film Sense FS-1 multi-wavelength ellipsometer. Cauchy models were used to model the native silicon oxide and the film. For the roughest films, a roughness layer on the film surface was included in the model using effective medium approximation with 50% void content. Thickness mapping using the ellipsometer was performed for selected samples by measuring film thickness at points separated by 0.5 cm (0.5 cm edge exclusion), resulting in 81 measurements over the 5 × 5 cm^2 silicon substrates. Energy-dispersive X-ray spectroscopy (EDS, Oxford INCA connected to a Hitachi S-4800 SEM) and X-ray reflectivity (XRR, Rigaku Smartlab) were also used for some samples to confirm the ellipsometry thicknesses, as shown in the Supporting Information (Figure S1–S5). For EDS, the thicknesses were calculated from Mo and W Lα k-ratios using GMRFilm software,[60]

assuming MO_3 stoichiometry and bulk densities (MoO_3 4.7 g/cm³, WO_3 7.2 g/cm³).[61] XRR was also used to determine film densities.

Film morphology was studied by scanning electron microscopy (SEM, Hitachi S-4800) and atomic force microscopy (AFM, Veeco Multimode V). Silicon probes with a tip radius of less than 10 nm (Bruker) were used for the tapping mode AFM imaging. The images were flattened to remove artefacts caused by sample tilt and scanner nonlinearity. Film roughness was calculated as a root mean square value (R_q) from 2 × 2 μm² images.

Film crystallinity was examined by X-ray diffraction (XRD, Rigaku Smartlab) using Cu Kα (λ = 1.54 Å) x-ray beam and either grazing incidence (incident angle of 1°) or θ-2θ geometry. Raman spectroscopy was performed in backscattering geometry using a confocal Raman microscope (NT-MDT Ntegra) with a 100× objective and a 532 nm or 633 nm laser.

Film composition was analyzed by time-of-flight elastic recoil detection analysis (ToF-ERDA) using a 40 MeV $^{79}Br^{7+}$ ion beam. The incident angle of the ion beam was 20° with respect to the sample surface. The angle between the sample and the detector was also 20°, resulting in a scattering angle of 40°. Valence and core level X-ray induced photoelectron spectra were measured at Dortmund Electron Accelerator (DELTA) using synchrotron based X-ray radiation of varied energy: 400 eV for Mo 3d and C 1s and 630 eV for O 1s core levels, 65 eV for valence band analysis, and 400, 630, or 650 eV for survey spectra. Two electron take-off angles of 0 or 60° with respect to the sample normal were used. The 60° take-off angle significantly increased surface sensitivity by probing less than half the depth of the 0° measurement. 5 eV pass energy and 0.5 eV (survey) or 0.05 eV (core and valence levels) step size were used. Sample surface was cleaned gently prior to measurements using low-energy Ar^+ ions at 0.5 kV accelerating voltage for 15 s. During the measurements, the chamber pressure was maintained at approximately 2×10^{-10} mbar. The C 1s peak at 284.5 eV was used as an energy reference. The peak deconvolution was performed using Gaussian functions with Shirley background removal taking into account the spin orbit splitting and the ratios of the corresponding quantum states.

Temperature-dependent resistivity measurements were performed under atmospheric conditions using the van der Pauw (vdP) four-point geometry for MoO_x samples deposited on 500 nm SiO_2/Si substrates. A similar MoO_x/500 nm SiO_2/Si structure with two silver (Ag) point contacts was used for hydrogen (H_2) sensing experiments. The gas atmosphere was controlled using mass flow controllers (MFCs, Bronkhorst Instruments) for hydrogen as well as for dry air that was used as the reference and balance gas. A Preama 5017 Digital Multimeter was used to measure current in a two-point configuration. In-house developed Labview software was used to control the flow rates of the testing and reference gases and to acquire the temperature and electrical current data. In all tests, the total flow was set to 50 sccm by mixing H_2 and dry air in defined proportions. H_2 concentration was varied from 5000 to 35000 ppm (0.5 to 3.5 vol-%). 15 minute pulses of H_2 were mostly used with 15 minute pulses of dry air in between to allow the sensor surface to recover before the next measurement.

Results and Discussion

Bis(tert-butylimido)bis(*N,N'*-diisopropylacetamidinato) compounds of both molybdenum and tungsten are solids that exhibit reasonably high and nearly identical volatility as shown by thermogravimetric analysis (TGA) in Figure 1. The residues of less than 3% at 500 °C suggest good thermal stability. The precursor temperatures needed to obtain sufficient vapor pressure for deposition experiments were estimated to be close to 150 °C for both compounds based on the previously developed empirical relation for our ALD reactor and TG instrument,[62] which was further refined to 145 °C for $[Mo(N^tBu)_2(dpamd)_2]$ and 155 °C for $[W(N^tBu)_2(dpamd)_2]$.

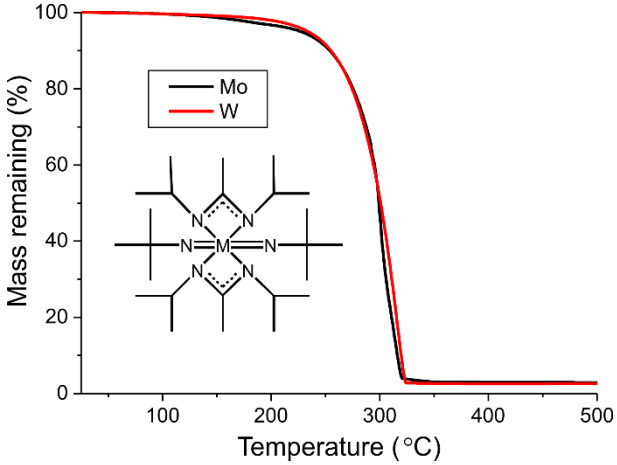

Figure 1. Thermogravimetric analysis of $[M(N^tBu)_2(dpamd)_2]$ compounds, where M = Mo (black) and W (red), heated under atmospheric pressure of N_2. The inset shows the schematic structure of the compounds.

We evaluated the reactivity of both compounds with different typical ALD reactants, including H_2O and O_3, H_2S, and NH_3 aiming to deposit oxides, sulfides, and nitrides, respectively. However, below the temperatures where the metal precursors were visually observed to decompose in the glass tubes of the ALD reactor, namely 300 °C for the Mo and 325 °C for the W precursor, films were only obtained using O_3 as the reactant. This suggests that the hydrides (H_2O, H_2S, and NH_3) are unable to protonate the ligands of the adsorbed precursors, whereas ozone is capable of combusting the ligands. Thus, we focused on the deposition of oxide films using O_3. Other compounds of molybdenum and tungsten could likely be deposited using more reactive, perhaps plasma-activated reactants.

Initial deposition studies at 300 °C showed a high growth rate, around 1.5 Å/cycle, using $[Mo(N^tBu)_2(dpamd)_2]$ and O_3, compared to 0.45 Å/cycle with $[W(N^tBu)_2(dpamd)_2]$ and O_3. However, saturation of the growth rate after a sufficient precursor dose is supplied, a unique characteristic of ALD, was not fully reached for molybdenum oxide when lengthening the

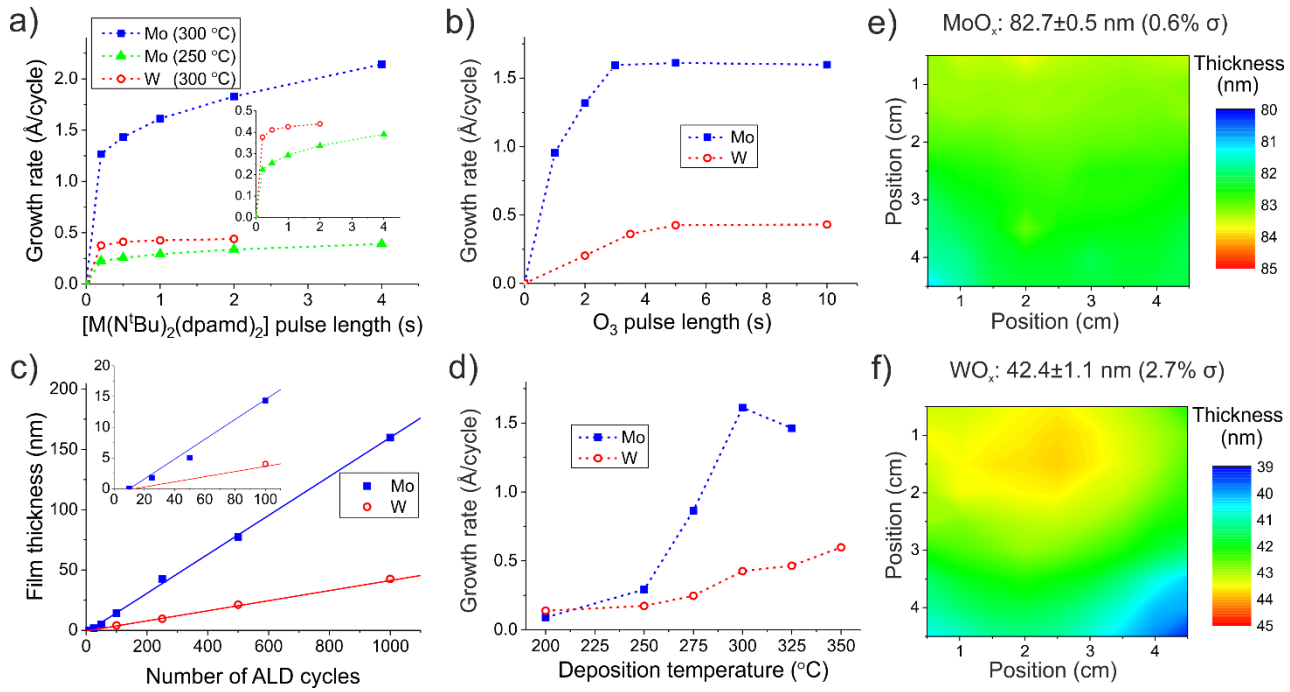

Figure 2. Growth rates of MoO_x and WO_x films versus a) $[M(N^tBu)_2(dpamd)_2]$ (inset shows region below 0.5 Å/cycle in more detail) and b) O_3 pulse length. c) Film thickness as a function of ALD cycles with inset showing the first 100 cycles in more detail. d) Growth rate versus deposition temperature. Ellipsometry thickness maps of e) MoO_x and f) WO_x films with 0.5 cm edge exclusion, where the precursor inlet and outlet are at the top and bottom of the figures, respectively. Unless otherwise noted, the films were deposited at 300 °C using 1000 cycles with 1 s $[M(N^tBu)_2(dpamd)_2]$ and 5 s O_3 pulses separated by 1 s N_2 purges. The thicknesses were measured by ellipsometry, see Supporting Information for EDS and XRR results (Figure S1–S5). Solid lines represent linear fits to the data and dashed lines are meant to guide the eye.

$[Mo(N^tBu)_2(dpamd)_2]$ pulse at 300 °C or even at 250 °C (Figure 2a), the latter being well below the decomposition temperature of the precursor as discussed below.

With O_3 the growth rate saturated when pulses of at least 3 s were used (Figure 2b). In contrast, for tungsten oxide, saturation at 0.45 Å/cycle was achieved with both precursors using $[W(N^tBu)_2(dpamd)_2]$ and O_3 pulses of at least 1 and 5 s, respectively (Figure 2 a,b). All further depositions were done using 1 s $[M(N^tBu)_2(dpamd)_2]$ and 5 s O_3 pulses separated by 1 s purges, unless otherwise noted.

The behavior of $[Mo(N^tBu)_2(dpamd)_2]$ is similar to our earlier studies on $[MoO_2(thd)_2]$ and O_3, where the growth rate did not completely saturate with the $[MoO_2(thd)_2]$ pulse, even though no film was deposited when only $[MoO_2(thd)_2]$ was pulsed.[48] Here, the observed increase of the growth rate when lengthening the Mo precursor pulse at 300 °C (~0.2 Å/cycle per additional 1 s of $[Mo(N^tBu)_2(dpamd)_2]$ pulsing) greatly exceeded the decomposition observed when only $[Mo(N^tBu)_2(dpamd)_2]$ was pulsed on silicon (~0.02 Å/cycle for 1 s pulses). This suggests precursor decomposition on the surface of the growing MoO_x film as the main reason for the lack of saturation as opposed to decomposition on the starting SiO_2 surface or in the gas phase. Furthermore, no film growth (decomposition) was observed when pulsing only $[Mo(N^tBu)_2(dpamd)_2]$ on silicon at 250 °C, yet the growth of MoO_x films was not saturative at this temperature, either. Therefore, MoO_x surface appears to have a catalytic effect in decomposition of the adsorbed $[Mo(N^tBu)_2(dpamd)_2]$.

Both processes exhibited linear growth when the number of ALD cycles was varied, although the intersection of the fitted lines and the x-axis at approximately 10 cycles suggests slight nucleation delay (Figure 2c). Notably, the linear growth behavior of MoO_x is in contrast to the previous two ALD processes capable of depositing crystalline MoO_x films, where initial slow growth of amorphous films was followed by faster growth after crystallization.[40,48]

Strong temperature dependence of the growth rate was evident for both processes, even more so for MoO_x with the growth rate increasing from 0.1 Å/cycle at 200 °C to 1.6 Å/cycle at 300 °C, whereas for WO_x the growth rate increased rather linearly from 0.2 Å/cycle at 200–250 °C to 0.6 Å/cycle at 350 °C (Figure 2d). The glass source tubes inside the ALD reactor revealed the first visual signs of metal precursor decomposition at 300 °C for $[Mo(N^tBu)_2(dpamd)_2]$, although film uniformity suffered only at 350 °C. With $[W(N^tBu)_2(dpamd)_2]$, decomposition was observed on the walls of the source tubes at 325 °C and above, but even the films deposited at 350 °C were uniform over the substrates. The increase in the growth rate with increasing deposition temperature when operating below the decomposition temperatures of the precursors is likely due to crystallization behavior of the films as discussed later, although changes in reaction mechanisms cannot be ruled out.

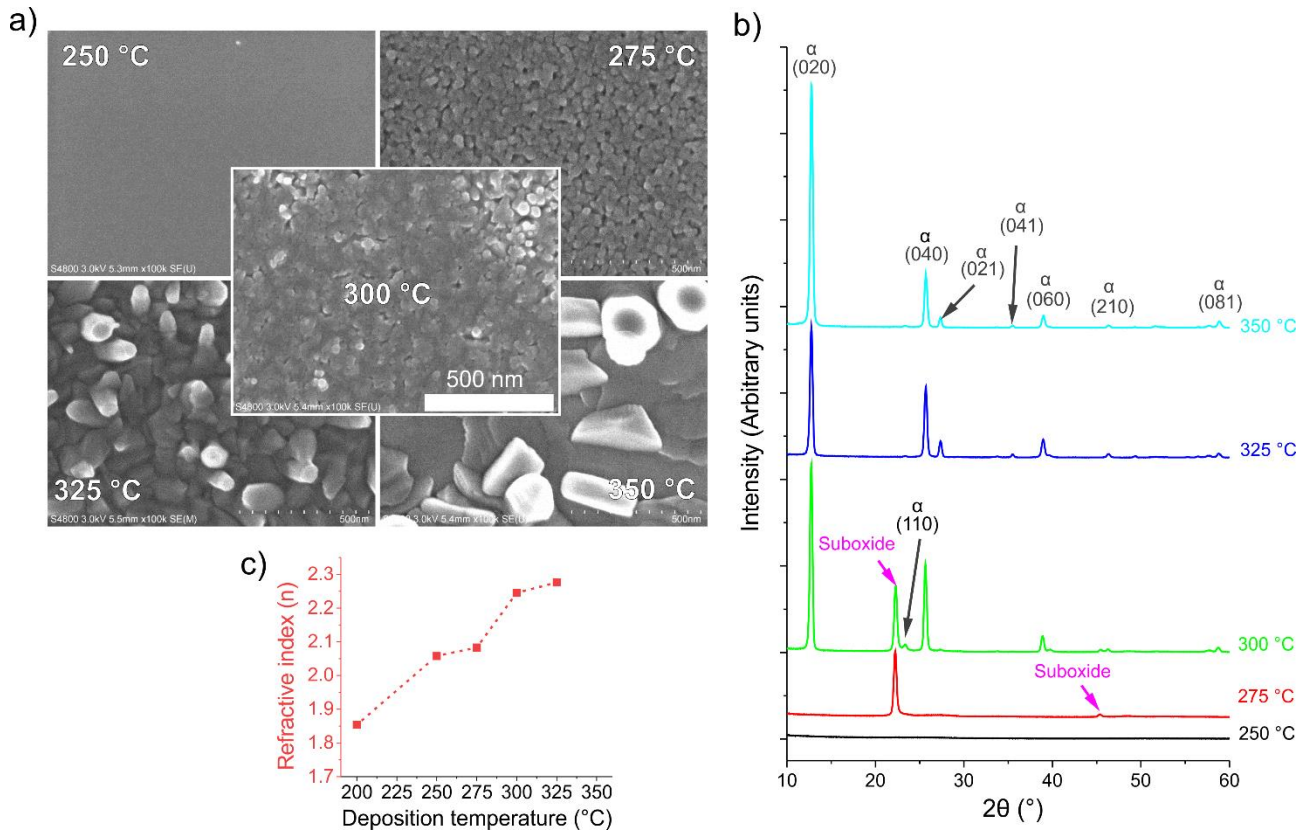

Figure 3. a) SEM images, b) grazing incidence X-ray diffractograms, and c) refractive indices (ellipsometry, at 630 nm) of MoO_x films deposited at different temperatures using 1000 cycles. α refers to α-MoO_3 (PDF 005-0508).

Both processes yielded very uniform films at 300 °C. The uniformity of the MoO_x films was remarkable – even though the growth rate did not completely saturate, the films had non-uniformity as low as 0.6% over the 5 × 5 cm^2 substrates (Figure 2e).The research-scale cross-flow reactor used in this work typically results in higher non-uniformities compared to many other ALD reactor designs due to inlet effects caused by byproduct readsorption and impurities in the carrier gas, for example.[34,36] For comparison, the $AlMe_3$+H_2O process, which is regarded as a near-ideal, model ALD process,[63] resulted in a non-uniformity of 0.8 % in our ALD reactor at 300 °C. The WO_x films were also uniform with a 2.7% non-uniformity measured for an approximately 40 nm film deposited at 300 °C (Figure 2f).

Conformality, the unique ability of ALD to uniformly coat complex structures, was studied by depositing a MoO_x film in a deep trench structure. Good, approximately 90% conformality was achieved up to an aspect ratio of 20 using the relatively short pulse and purge lengths selected for this experiment, although a change in film morphology as a function of the aspect ratio was observed (Figure S6 in Supporting Information).

The strong temperature-dependence of the MoO_x film growth may be explained by changes in film crystallinity and morphology. The films deposited at 250 °C and below were very smooth, while the films deposited at 275 °C and above were clearly rougher (Figure 3a). Whereas the films deposited at 275 and 300 °C still had a relatively compact and smooth-looking surface, those deposited at 325 °C and especially 350 °C appeared very rough with tall rod-like grains present on the surface, in line with the matte-like visual appearance of the film deposited at 350 °C.

The morphology was also correlated with the film crystallinity (Figure 3b): the smooth films deposited at 250 °C and below were amorphous, whereas at 275 °C a strong X-ray reflection emerged at 22.2 °2θ accompanied by a weaker one at 45.4°, which corresponds to half of the d-spacing of the first reflection. These reflections are suggested to originate from a crystalline suboxide MoO_x phase ($2.75 \leq x \leq 2.89$). Based on the peak positions, the most likely candidate is the orthorhombic γ-Mo_4O_{11} (Powder Diffraction File, PDF 005-0337), although other suboxide phases also have reflections within ±0.3° of 22.2°, including monoclinic η-Mo_4O_{11} (PDF 013-0142), $Mo_{17}O_{47}$ (PDF 013-0345), Mo_5O_{14} (PDF 012-0517), Mo_8O_{23} (PDF 005-0339), and Mo_9O_{26} in both triclinic (PDF 012-0753) and monoclinic (PDF 005-0441) forms. Thus, the suboxide phase could not be definitively identified by XRD. We were also unable to identify the suboxide phase by Raman spectroscopy (Figure S7 and Table S1 in Supporting Information).

In the samples made at 300 °C, reflections of the stable orthorhombic α-MoO_3 (PDF 005-0508) appeared in addition to the suboxide reflections. The films deposited at 325 to 350 °C were phase-pure α-MoO_3. θ-2θ XRD measurements showed the α-MoO_3 to be preferentially oriented with the (0k0) planes parallel to the substrate (Figure S9 in Supporting Information). Previously, a three-phase mixture of a suboxide phase and both α and β-MoO_3 phases was observed in ALD MoO_x films deposited from

$[MoO_2(thd)_2]$ and O_3 at 225 to 260 °C, whereas nearly phase-pure α-MoO_3 films was deposited at 300 °C.[48] Thus, the onset of crystallization was about 50 °C higher in the present process compared to the $[MoO_2(thd)_2]+O_3$ process. In comparison, the PEALD process of Vos et al.[40] using $[Mo(N^tBu)_2(NMe_2)_2]$ and O_2 plasma produced crystalline α-MoO_3 films at 300–350 °C.

The refractive index (at 630 nm) increased with increasing deposition temperature from 1.85 at 200 °C to 2.3 at 325 °C (Figure 3c), which we attribute to densification and crystallization as well as changes in texture. Refractive indices of 1.8–2.2 at ~630 nm have been reported for trioxide-like MoO_x thin films.[40,64] For reference, the refractive index of bulk α-MoO_3 single crystals at 589 nm has been shown to be strongly anisotropic, ranging from 1.88 to 2.54 along the a and c axes, respectively.[65] XRR measurements showed that the amorphous films deposited at 250 °C had a rather low density of 3.6–3.7 g/cm^3 as compared to the MoO_3 bulk density of 4.7 g/cm^3.[61] Unfortunately, high roughness prevented density measurements of our crystalline MoO_x films by XRR.

Next, the effect of the MoO_x film thickness on the morphology and crystallinity was examined by varying the number of ALD cycles at 300 °C. The films started to roughen already after 50 cycles due to what appeared to be formation of crystallites on the surface (Figure 4a and Figure S9 in Supporting Information). Thereafter, the root-mean-square roughness remained nearly constant at 4 to 5 nm between 250 and 1000 cycles despite the four-fold increase in thickness. The morphology evolved from a surface pronouncedly exposing individual crystallites at 250 cycles to a more compact-looking surface at 1000 cycles. Grazing incidence X-ray diffraction (GIXRD) showed the first signs of the suboxide phase after 100 cycles, whereas α-MoO_3 started to form after 250 cycles. The relative amount of α-MoO_3 in comparison to the suboxide then increased with increasing number of cycles (GIXRD in Figure 4b and θ-2θ XRD in Figure S10 in Supporting Information)

In addition to the deposition temperature and film thickness, the phase composition could be modified by changing the precursor pulse lengths. Increasing the $[Mo(N^tBu)_2(dpamd)_2]$ pulse length at 300 °C increased the amount of the suboxide phase relative to α-MoO_3 and smoothened the film surface (Figure S11–S13 in Supporting Information), whereas O_3 pulse length had the opposite effect (Figure S14–S16 in Supporting Information). In particular, nearly phase-pure α-MoO_3 was obtained using the longest, 10 s O_3 pulses. Effects of pulse times on film composition, crystallinity, and other properties are rarely examined, especially in the saturative ALD regime. Nevertheless, these effects are certainly not unique to this process, as similar observations have been made in ALD MoO_x,[48] SnS,[66] and TiN[67] processes, for example.

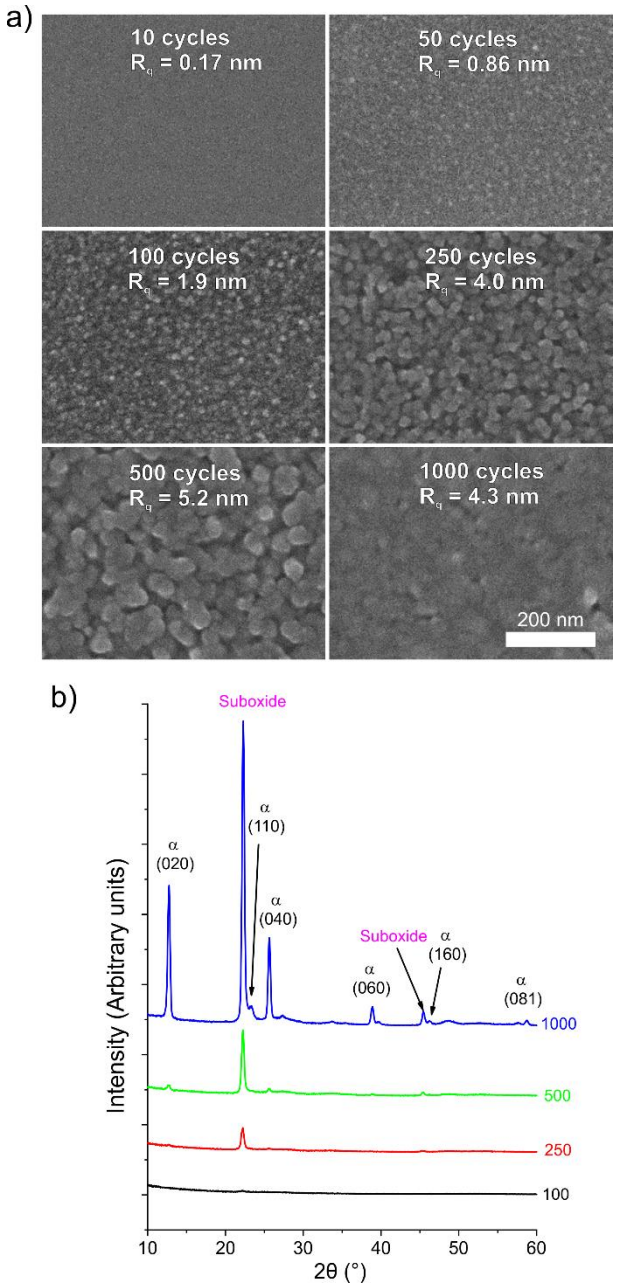

Figure 4. a) SEM images and roughness values (R_q) determined by AFM as well as b) grazing incidence X-ray diffractograms of MoO_x films deposited at 300 °C with different number of ALD cycles. α refers to α-MoO_3 (PDF 005-0508).

The morphology of the WO_x films was also strongly temperature-dependent. The films grown at 250 °C and below were smooth similar to the MoO_x films, whereas individual crystallites started to form on the film surface at 275 °C and above (Figure 5a). Only the films deposited at 325 to 350 °C appeared to be fully crystalline, however. Thus, the crystallization of WO_x seems to occur at slightly larger thicknesses and temperatures compared to MoO_x.

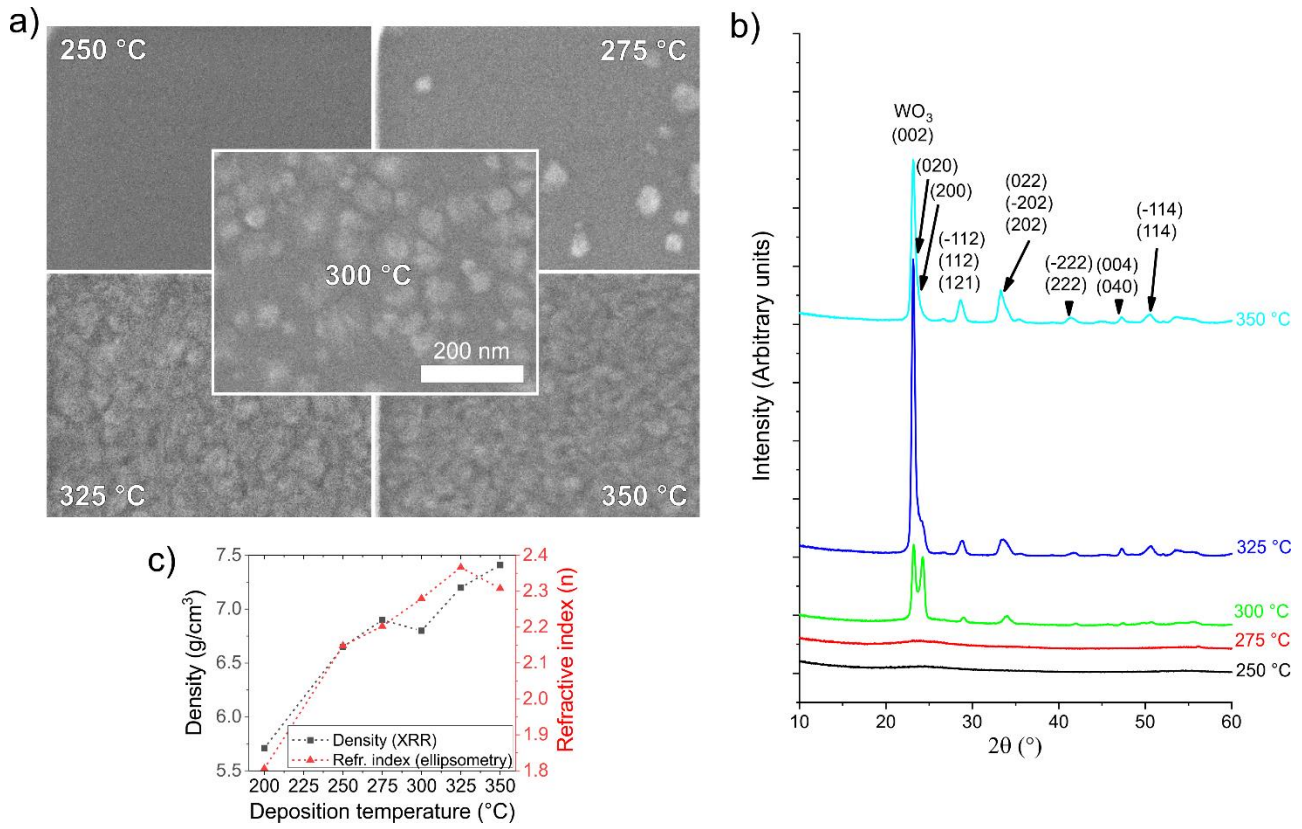

Figure 5. a) SEM images, b) grazing incidence X-ray diffractograms, and c) refractive indices (ellipsometry, at 630 nm) and densities (XRR) of WO_x films deposited at different temperatures using 1000 cycles.

Furthermore, the crystalline WO_x films had a denser and smoother appearance compared to MoO_x. These interpretations are supported by GIXRD, which showed no signs of crystallinity at 250 °C, a very weak and broad peak at 275 °C, and sharp peaks attributed to WO_3 at 300 °C and above (Figure 5b). The films exhibited an increasing degree of preferred (002) orientation with increasing deposition temperature (Figure S17 in Supporting Information).

We indexed the reflections to the monoclinic γ-WO_3 phase (PDF 043-1035), which is stable from 17 to 350 °C in bulk form, although other phases of WO_3 including the triclinic δ-WO_3 (stable from -40 to 17 °C, PDF 20-1323) and the orthorhombic β-WO_3 (stable from 350 to 720 °C, PDF 020-1324) have similar structures and could not be definitively ruled out.[68] Contrary to MoO_x, no suboxide WO_x phases were seen in any of the films. Raman spectra of the WO_x films deposited at 300 °C and above only revealed modes attributed to one of the WO_3 phases (Figure S18 and Table S2 in Supporting Information).

Both the refractive indices (at 630 nm) and densities of the WO_x films increased with increasing deposition temperature, from 1.8 and 5.7 g/cm^3 at 200 °C, respectively, up to 2.3 and 7.4 g/cm^3 at 350 °C (Figure 5c). The refractive indices agree with reports on WO_3 thin films,[42,69] although even higher values from 2.28 to 2.70 along the c and a-axes, respectively, have been reported for bulk WO_3 single crystals at the long-wavelength limit.[70] The density of the films deposited at the highest temperatures is practically equivalent to the WO_3 bulk density of 7.2 g/cm^3.[61]

The thinnest WO_x film deposited using 100 cycles at 300 °C (approximately 4 nm) was smooth (Figure 6a) and amorphous (Figure 6b and Figure S19 in Supporting Information). A few small crystallites were visible on the surface after 250 cycles, but XRD detected crystallinity only after 500 cycles. After 1000 cycles at 300 °C the surface still had some smooth, likely amorphous areas.

The crystallinity of the WO_x films was also correlated to the precursor pulse lengths used, as was observed for the MoO_x films. The [$W(N^tBu)_2(dpamd)_2$] pulse length yielding the highest crystallinity and density at 300 °C was 0.5 s, below the length needed for the saturation (Figure S20–S22 in Supporting Information). On the other hand, lengthening the O_3 pulse length increased the crystallinity, density, refractive index, and the degree of the preferred (002) orientation (Figure S23–S25 in Supporting Information).

Both the MoO_x (Table 1) and WO_x (Table 2) films were relatively close to the MO_3 stoichiometry with low impurity contents according to ToF-ERDA. For the MoO_x films deposited at 275 °C the O/Mo stoichiometry of 2.80 was in line with the film being at least partly crystalline suboxide ($2.75 \leq x \leq 2.89$), whereas the α-MoO_3 film deposited at 325 °C had an excess of oxygen (O/Mo 3.19). The C and N levels, likely originating from the precursor ligands, were low and generally decreased with increasing deposition temperature. The somewhat higher hydrogen content in the MoO_x films (1.4–2.7 at.%) showed little

Table 1. Composition of MoO_x films deposited using 1000 cycles as determined by ToF-ERDA.

T (°C)	Mo (at.%)	O (at.%)	O / Mo	C (at.%)	N (at.%)	H (at.%)
275	25.3±0.3	70.8±0.9	2.80±0.05	0.62±0.09	1.27±0.12	2.0±0.4
300	23.5±0.2	72.6±0.6	3.09±0.04	0.19±0.03	1.03±0.08	2.7±1.2
325	23.4±0.3	74.6±0.8	3.19±0.05	0.33±0.06	0.36±0.05	1.4±0.3

Table 2. Composition of WO_x films deposited using 1000 cycles as determined by ToF-ERDA.

T (°C)	W (at.%)	O (at.%)	O / W	C (at.%)	N (at.%)	H (at.%)
300	25.3±0.3	73.4±1.9	2.90±0.08	0.38±0.14	0.48±0.13	0.39±0.21
350	25.0±0.2	73.7±1.3	2.95±0.06	0.40±0.09	0.32±0.08	0.61±0.23

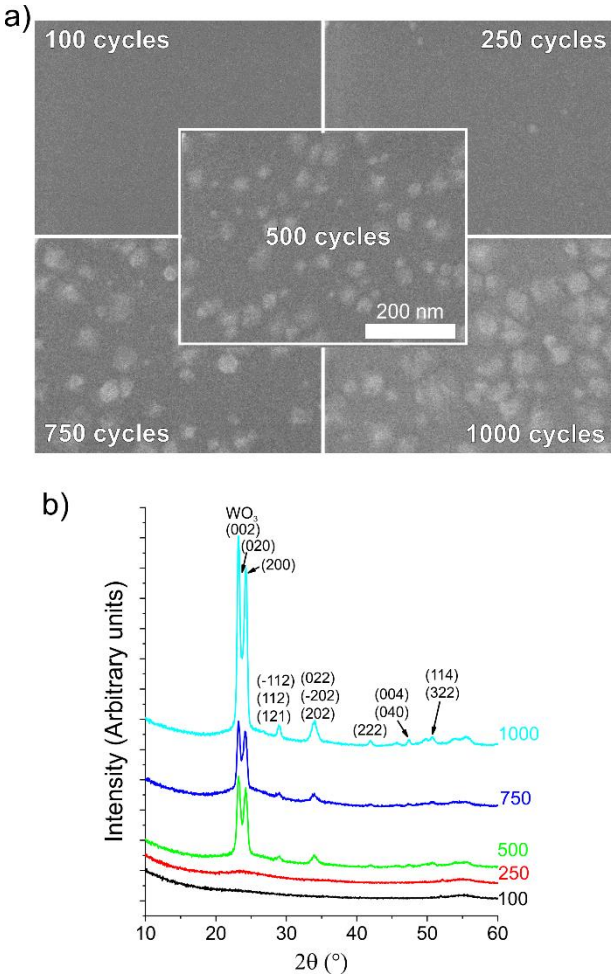

Figure 6. a) SEM images and b) grazing incidence X-ray diffractograms of WO_x films deposited with different number of ALD cycles at 300 °C.

correlation with carbon and nitrogen and is thus attributed to hydroxyl (OH^-) groups, which would also explain some of the excess oxygen in the films. The WO_x films deposited at both 300 and 350 °C were close to the WO_3 stoichiometry (O/W 2.9–2.95) with very low impurity contents; only about 1.3 at.% of C, N, and H combined. The impurity contents were lower or on similar level compared to the reported ALD MoO_x[40,48] and WO_x[38,42] films.

In order to gain further insight into the structure and composition of the scarcely studied suboxide MoO_x films, we used synchrotron photoemission spectroscopy to characterize a 50 nm molybdenum oxide film deposited at 275 °C. Measurements were done after gentle Ar^+ sputtering using two take-off angles, 0 and 60° with respect to the surface normal, the latter resulting in increased surface sensitivity. Survey scans detected only Mo, O, and C, the last one being a surface contaminant (Figure S26 in Supporting Information). The broad Mo 3d doublet at 0° take-off angle was deconvoluted to three chemical states (Figure 7a): Mo^{6+}, Mo^{5+}, and Mo^{4+} with Mo $3d_{5/2}$ binding energies (and relative amounts) of 233.0 eV (28%), 231.6 eV (51%), and 230.2 eV (21%), respectively (Table S3 in Supporting Information).[32,71,72] Compared to the $MoO_{2.8}$ composition determined by ToF-ERDA as an average through the film thickness, photoemission spectroscopy yielded a more oxygen-deficient composition: $MoO_{2.6}$ and $MoO_{2.4}$ at 0° and 60° take-off angles, respectively, which suggests that the oxidation state of molybdenum and the O/Mo ratio were lower on the film surface than in the film bulk. The surface composition may have changed while cooling the film in vacuum after the film deposition or during storage in air.

Five main chemical states were identified in the O 1s spectra (Figure 7a) at 534.4 eV (adsorbed H_2O), 533.7 eV (surface OH^-), 532.8 eV (O^{2-} bonded with Mo^{4+}), 531.5 eV (O^{2-} bonded with Mo^{5+}), and 530.6 eV (O^{2-} bonded with Mo^{6+}). The valence band spectra show convoluted Mo 4d and 5s as well as O 2p features between 5 and 15 eV and O 2s levels near 23 eV (Figure 7b). The defect states located at approximately 3 eV below the Fermi level were attributed to oxygen vacancies of the MoO_x film, which are more pronounced on the surface (60° take-off angle).

The valence band maximum was located at 1.0 eV below the Fermi level. We estimated the work function of the film by extrapolating the linear part of the secondary electron cut-off to zero and deducting this from the excitation photon energy of 65 eV (not shown). This procedure yielded values of 6.0 and 7.0 eV at 0 and 60° take-off angles, respectively. The higher work function at the 60° take-off angle is attributed to surface contamination and hydroxyl groups, whereas the value of 6.0 eV obtained at 0° matches those reported for non-stoichiometric MoO_x.[73–75]

Next, to explore the suitability of MoO_x films for gas sensing, we performed temperature-dependent resistivity measurements in air on 50 nm MoO_x films deposited at

275 and 300 °C, which consisted of the suboxide and a mixture of the suboxide and α-MoO_3 phases, respectively (Figure S27 in Supporting Information). Both films had a resistivity of approximately 80 Ωcm at 40 °C (Figure 8). The resistivity first increased up to 76 °C, likely due to desorption of H_2O, and then decreased at higher temperatures as expected for semiconductors. The film deposited at 300 °C had a higher resistivity between 115 and 189 °C than the film deposited at 275 °C probably due to the greater oxygen deficiency of the latter.

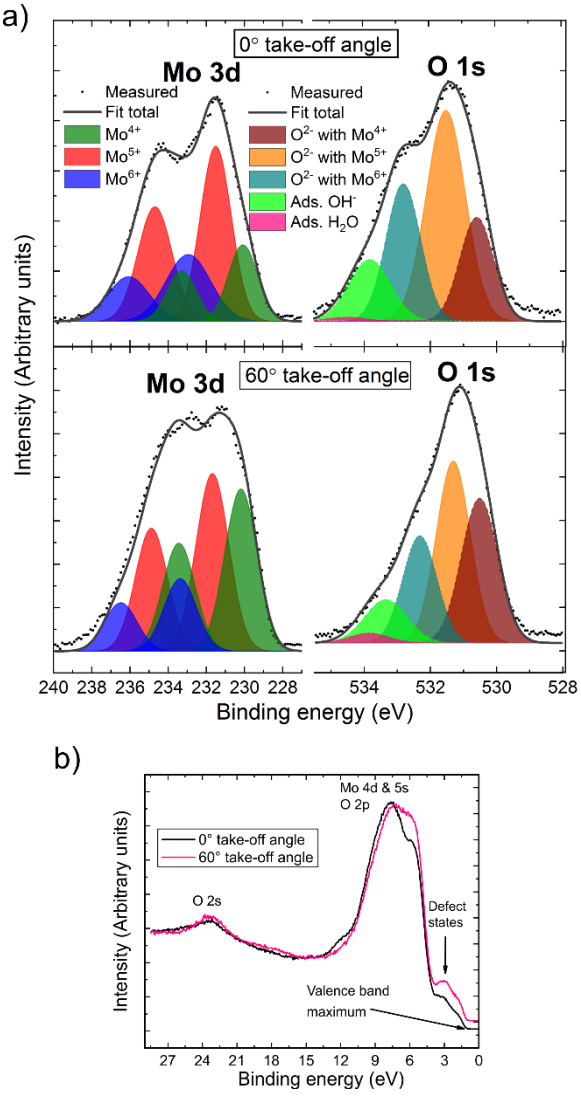

Figure 7. a) High resolution Mo 3d and O 1s X-ray photoemission spectra and b) valence band region of a 50 nm MoO_x films deposited at 275 °C measured at 0 and 60° take-off angles.

Above 200 °C the difference between the samples decreased, likely due to annealing of surface defects. Both films ended up having a resistivity of 6–7 Ωcm at 330 °C. Identical results were obtained on cooling the film and repeating the measurements, which shows that no irreversible changes in film structure occurred up to 330 °C.

The measured resistivity values are relatively low compared to stoichiometric MoO_3, which has a resistivity above 10^9 Ωcm at room temperature.[76,77] Various suboxides have been reported to have much lower resistivities compared to MoO_3, ranging from 100 Ωcm for Mo_9O_{26} to as low as 10^{-4} Ωcm for γ-Mo_4O_{11}.[8,9] Additionally, easily forming oxygen vacancies are known to greatly enhance the conductivity of MoO_3.[1]

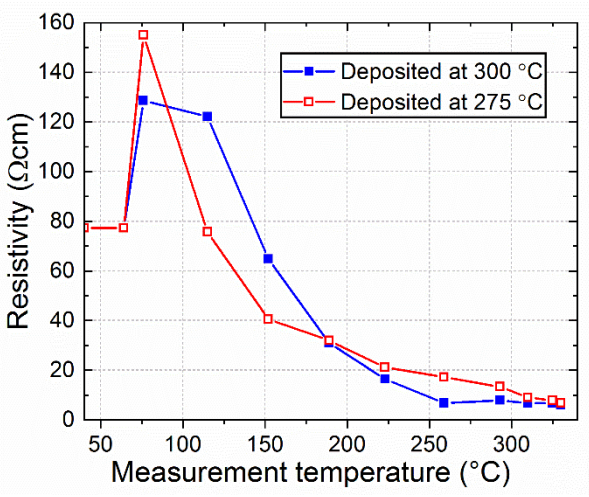

Figure 8. Resistivity versus temperature (in air) of 50 nm MoO_x films deposited at 275 and 300 °C on 500 nm SiO_2/Si substrates.

Finally, a simple gas sensor device was constructed by depositing a 50 nm MoO_x film at 275 °C on a silicon substrate covered with 500 nm of SiO_2. The device was contacted using two silver point contacts. The 275 °C sample was chosen because of its phase composition: as described above, the films deposited at 275 °C contained an unidentified molybdenum suboxide phase as the only crystalline phase and had surface and bulk stoichiometries of $MoO_{2.4}$ and $MoO_{2.8}$ according to synchrotron-based XPS and ToF-ERDA, respectively. Unlike MoO_3,[25–30] molybdenum suboxides have not, to the best of our knowledge, been previously studied as hydrogen gas sensor materials.

The MoO_x sensor exhibited a clear, reversible change in conductance when exposed to different concentrations of hydrogen gas. The response against H_2 was quantified using the absolute value of sensitivity (S), which represents the change in conductance compared to that measured in dry air as defined in Eq. 1, where C_E and C_B denote conductance during exposure to the target gas and baseline in dry air, respectively. Additionally, response (recovery) times were defined as the time passed until the sensor reached 90% (10%) of the maximum signal for a given concentration. Furthermore, following a common convention, a decrease in conductance when exposed to hydrogen is designated as p-type response and an increase is termed n-type response.[78]

$$\text{Sensitivity (S)} = \left[\left(\frac{|C_E - C_B|}{C_B}\right) \times 100\right] \qquad \text{Equation 1}$$

The MoO_x sensor showed an overall p-type response to hydrogen when the sensor was operated at 120 °C. During each hydrogen pulse the sensor exhibited a weak initial n-type response, in other words an increase in conductance, but a much stronger p-type response, i.e. decrease in conductance quickly followed leading to an overall p-type response of the sensor. The semiconducting molybdenum

oxides usually behave as n-type semiconductors and gas sensors.[25–30] Although p-type response has also been reported for MoO_3 gas sensors,[32] reasons for the p-type behavior are not understood at present.

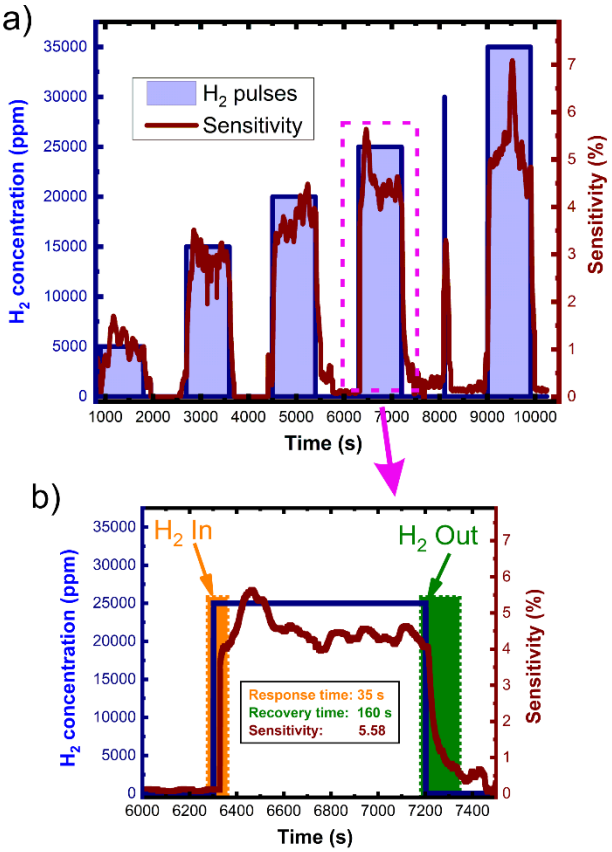

Figure 9. Dynamic sensor response of a 50 nm MoO_x film deposited at 275 °C: a) complete measurement against six different concentrations of H_2 (5000–35000 ppm) and two different exposure times (1 and 15 min) and b) a more detailed view of the 15 min 25000 ppm H_2 pulse along with the extracted sensor performance. The measurements were done at 120 °C.

The sensitivity increased from 1.6 to 6.9% when the H_2 concentration increased from 5000 to 35000 ppm (Figure 9a). The sensor responded rapidly to the changes in the atmosphere with response and recovery times of 36 and 160 s determined during a 15 minute 25000 ppm H_2 pulse (Figure 9b). Even a one-minute pulse of H_2 resulted in a sensitivity of 3.2% at 30000 ppm H_2 concentration. Thus, the sensor showed fast kinetics as well as a repeatable and reversible response with a capability to distinguish between different hydrogen concentrations at a relatively low operating temperature of only 120 °C. Future work is planned with more sophisticated interdigitated current collectors (IDEs) in order to obtain more detailed information on the sensing mechanisms as well as to use higher testing temperatures to increase the sensitivity.

Conclusions

We introduced bis(tert-butylimido)bis(*N,N'*-diisopropylacetamidinato) compounds of molybdenum and tungsten as precursors for atomic layer deposition. MoO_x and WO_x ($x \approx 3$) films were deposited using ozone as a reactant at 200 to 350 °C. Both precursors yielded uniform films, although the growth behaviors differed: MoO_x films grew at a high growth rate of up to 2 Å/cycle at 300 °C but without complete saturation, whereas the growth of WO_x was saturative with a growth rate of 0.45 Å/cycle at 300 °C. Crystallinity and composition could be tuned by changing deposition conditions, especially the deposition temperature, but also film thickness and precursor pulse times. Whereas WO_x crystallized to WO_3 at 300 °C and above, MoO_x formed crystalline suboxide (275–300 °C) and α-MoO_3 (300–350 °C) phases. Crystalline films of both metal oxides were very pure and close to the expected stoichiometry. Synchrotron-based surface enhanced photoemission spectroscopy revealed a high amount of oxygen vacancies on the surface of a MoO_x suboxide film deposited at 275 °C. The temperature-dependent resistivity of the MoO_x films suggested the films to be suitable for gas sensor applications. A simple hydrogen gas sensor device constructed using a 50 nm suboxide MoO_x film showed reversible and fast response to hydrogen gas at low temperature. The present results form a solid base for further in-depth studies exploring the use of uniform and conformal molybdenum and tungsten oxide films with controlled crystallinity as gas sensors as well as in other applications, such as catalysis and energy storage.

ASSOCIATED CONTENT

Supporting Information. Thickness measurements using different methods (ellipsometry, EDS, and XRR), SEM images of MoO_x film deposited in a trench structure. Further XRD and Raman data of MoO_x and WO_x films deposited at different temperatures and with different number of ALD cycles. AFM images of MoO_x films deposited at 300 °C. SEM images, X-ray diffractograms, and refractive indices of MoO_x and WO_x films deposited using different precursor pulse lengths. Photoelectron survey spectra, tabulated photoemission results, X-ray diffractograms and SEM images of a 50 nm MoO_x film deposited at 275 °C. This material is available free of charge via the Internet at http://pubs.acs.org.

AUTHOR INFORMATION

Corresponding Authors

*M. Mattinen. E-mail: miika.mattinen@helsinki.fi
*M. Ritala. E-mail: mikko.ritala@helsinki.fi

Author Contributions

The manuscript was written through contributions of all authors.

Notes

The authors declare no competing financial interest.

ACKNOWLEDGMENT

The research was supported by ASM Microchemistry and the Finnish Centre of Excellence in Atomic Layer Deposition (ALDCoE) funded by the Academy of Finland. The authors from Ruhr-University Bochum and Heinrich Heine University Düsseldorf acknowledge the funding from European Funds for Regional Development (EFRE-0800672-FunALD).

Alexander Sadlo, Martin Wilken and Annika Krusenbaum are acknowledged for synthesizing the precursors. We acknowledge the use of DELTA (Dortmund Electron Accelerator) for synchrotron based photoemission measurements. We also extend our sincere thanks to Ph.D. students Karim Shamout and Peter Roese and Prof. Dr. Carsten Westphal.

REFERENCES

(1) de Castro, I. A.; Datta, R. S.; Ou, J. Z.; Castellanos-Gomez, A.; Sriram, S.; Daeneke, T.; Kalantar-zadeh, K. Molybdenum Oxides – From Fundamentals to Functionality. *Adv. Mater.* **2017**, *29*, 1701619.

(2) Huang, Z.-F.; Song, J.; Pan, L.; Zhang, X.; Wang, L.; Zou, J.-J. Tungsten Oxides for Photocatalysis, Electrochemistry, and Phototherapy. *Adv. Mater.* **2015**, *27*, 5309–5327.

(3) Zheng, H.; Ou, J. Z.; Strano, M. S.; Kaner, R. B.; Mitchell, A.; Kalantar-zadeh, K. Nanostructured Tungsten Oxide - Properties, Synthesis, and Applications. *Adv. Funct. Mater.* **2011**, *21*, 2175–2196.

(4) Kihlborg, L. Studies on Molybdenum Oxides. *Acta Chem. Scand.* **1959**, *13*, 954–962.

(5) Kihlborg, L. The Crystal Chemistry of Molybdenum Oxides. In *Advances in Chemistry: Nonstoichiometric Compounds*; Ward, R., Ed.; American Chemical Society: Washington, D.C., 1963; Vol. 39, pp 37–45.

(6) Tilley, R. J. D. The Crystal Chemistry of the Higher Tungsten Oxides. *Int. J. Refract. Met. Hard Mater.* **1995**, *13*, 93–109.

(7) Migas, D. B.; Shaposhnikov, V. L.; Borisenko, V. E. Tungsten Oxides. II. The Metallic Nature of Magnéli Phases. *J. Appl. Phys.* **2010**, *108*, 093714.

(8) Smith, R. L.; Rohrer, G. S. Scanning Probe Microscopy of Cleaved Molybdates: α-MoO_3(010), $Mo_{18}O_{52}$(100), Mo_8O_{23}(010), and η-Mo_4O_{11}(100). *J. Solid State Chem.* **1996**, *124*, 104–115.

(9) da Luz, M. S.; de Campos, A.; White, B. D.; Neumeier, J. J. Electrical Resistivity, High-Resolution Thermal Expansion, and Heat Capacity Measurements of the Charge-Density Wave Compound γ-Mo_4O_{11}. *Phys. Rev. B* **2009**, *79*, 233106.

(10) Rogers, D. B.; Shannon, R. D.; Sleight, A. W.; Gillson, J. L. Crystal Chemistry of Metal Dioxides with Rutile-Related Structures. *Inorg. Chem.* **1969**, *8*, 841–849.

(11) Kanu, S. S.; Binions, R. Thin Films for Solar Control Applications. *Proc. R. Soc. A.* **2009**, *466*, 19–44.

(12) Bettahar, M. M.; Costentin, G.; Savary, L.; Lavalley, J. C. On the Partial Oxidation of Propane and Propylene on Mixed Metal Oxide Catalysts. *Appl. Catal. A* **1996**, *145*, 1–48.

(13) Dong, P.; Hou, G.; Xi, X.; Shao, R.; Dong, F. WO_3-Based Photocatalysts: Morphology Control, Activity Enhancement and Multifunctional Applications. *Environ. Sci. Nano* **2017**, *4*, 539–557.

(14) Szilágyi, I. M.; Fórizs, B.; Rosseler, O.; Szegedi, Á.; Németh, P.; Király, P.; Tárkányi, G.; Vajna, B.; Varga-Josepovits, K.; László, K. Tóth, A. L.; Baranyai, P.; Leskelä, M. WO_3 Photocatalysts: Influence of Structure and Composition. *J. Catal.* **2012**, *294*, 119–127.

(15) Long, H.; Zeng, W.; Zhang, H. Synthesis of WO_3 and Its Gas Sensing: A Review. *J. Mater. Sci:. Mater. Electron.* **2015**, *26*, 4698–4707.

(16) Eranna, G.; Joshi, B. C.; Runthala, D. P.; Gupta, R. P. Oxide Materials for Development of Integrated Gas Sensors - A Comprehensive Review. *Crit. Rev. Solid State Mater. Sci.* **2004**, *29*, 111–188.

(17) Arita, M.; Kaji, H.; Fujii, T.; Takahashi, Y. Resistance Switching Properties of Molybdenum Oxide Films. *Thin Solid Films* **2012**, *520*, 4762–4767.

(18) Jeong, D. S.; Thomas, R.; Katiyar, R. S.; Scott, J. F.; Kohlstedt, H.; Petraru, A.; Hwang, C. S. Emerging Memories: Resistive Switching Mechanisms and Current Status. *Rep. Prog. Phys.* **2012**, *75*, 076502.

(19) Ji, Y.; Yang, Y.; Lee, S.-K.; Ruan, G.; Kim, T.-W.; Fei, H.; Lee, S.-H.; Kim, D.-Y.; Yoon, J.; Tour, J. M. Flexible Nanoporous WO_{3-x} Nonvolatile Memory Device. *ACS Nano* **2016**, *10*, 7598–7603.

(20) Chernova, N. A.; Roppolo, M.; Dillon, A. C.; Whittingham, M. S. Layered Vanadium and Molybdenum Oxides: Batteries and Electrochromics. *J. Mater. Chem.* **2009**, *19*, 2526–2552.

(21) Song, J.; Huang, Z.-F.; Pan, L.; Zou, J.-J.; Zhang, X.; Wang, L. Oxygen-Deficient Tungsten Oxide as Versatile and Efficient Hydrogenation Catalyst. *ACS Catal.* **2015**, *5*, 6594–6599.

(22) Machiels, C. J.; Cheng, W. H.; Chowdhry, U.; Farneth, W. E.; Hong, F.; McCarron, E. M.; Sleight, A. W. The Effect of the Structure of Molybdenum Oxides on the Selective Oxidation of Methanol. *Appl. Catal.* **1986**, *25*, 249–256.

(23) Yao, D. D.; Ou, J. Z.; Latham, K.; Zhuiykov, S.; O'Mullane, A. P.; Kalantar-zadeh, K. Electrodeposited α- and β-Phase MoO_3 Films and Investigation of Their Gasochromic Properties. *Cryst. Growth Des.* **2012**, *12*, 1865–1870.

(24) Delmon, B. Solid State Reactions in Catalysts: An Approach to Real Active Sytems and Their Deactivation. In *Studies in Surface Science and Catalysis*; Bartholomew, C. H., Fuentes, G. A., Eds.; Elsevier B.V.: Amsterdam, Netherlands, 1997; Vol. 111, pp 39–51.

(25) Alsaif, M. M. Y. A.; Balendhran, S.; Field, M. R.; Latham, K.; Wlodarski, W.; Ou, J. Z.; Kalantar-zadeh, K. Two Dimensional α-MoO_3 Nanoflakes Obtained Using Solvent-Assisted Grinding and Sonication Method: Application for H_2 Gas Sensing. *Sens. Actuators B.* **2014**, *192*, 196–204.

(26) Rahmani, M. B.; Keshmiri, S. H.; Yu, J.; Sadek, A. Z.; Al-Mashat, L.; Moafi, A.; Latham, K.; Li, Y. X.; Wlodarski, W.; Kalantar-zadeh, K. Gas Sensing Properties of Thermally Evaporated Lamellar MoO_3. *Sens. Actuators B* **2010**, *145*, 13–19.

(27) Yang, S.; Wang, Z.; Hu, Y.; Luo, X.; Lei, J.; Zhou, D.; Fei, L.; Wang, Y.; Gu, H. Highly Responsive Room-Temperature Hydrogen Sensing of α-MoO_3 Nanoribbon Membranes. *ACS Appl. Mater. Interfaces* **2015**, *7*, 9247–9253.

(28) Luo, X.; You, K.; Hu, Y.; Yang, S.; Pan, X.; Wang, Z.; Chen, W.; Gu, H. Rapid Hydrogen Sensing Response and Aging of α-MoO_3 Nanowires Paper Sensor. *Int. J. Hydrogen Energy* **2017**, *42*, 8399–8405.

(29) Illyaskutty, N.; Kohler, H.; Trautmann, T.; Schwotzer, M.; Mahadevan Pillai, V. P. Hydrogen and Ethanol Sensing Properties of Molybdenum Oxide Nanorods Based Thin Films: Effect of Electrode Metallization and Humid Ambience. *Sens. Actuators B* **2013**, *187*, 611–621.

(30) Sunu, S. S.; Prabhu, E.; Jayaraman, V.; Gnanasekar, K. I.; Seshagiri, T. K.; Gnanasekaran, T. Electrical Conductivity and Gas Sensing Properties of MoO_3. *Sens. Actuators B* **2004**, *101*, 161–174.

(31) Galatsis, K.; Li, Y. X.; Wlodarski, W.; Comini, E.; Sberveglieri, G.; Cantalini, C.; Santucci, S.; Passacantando, M. Comparison of Single and Binary Oxide MoO_3, TiO_2 and WO_3 Sol-Gel Gas Sensors. *Sens. Actuators B* **2002**, *83*, 276–280.

(32) Çiftyürek, E.; Sabolsky, K.; Sabolsky, E. M. Molybdenum and Tungsten Oxide Based Gas Sensors for High Temperature Detection of Environmentally Hazardous Sulfur Species. *Sens. Actuators B* **2016**, *237*, 262–274.

(33) Wildfire, C.; Çiftyürek, E.; Sabolsky, K.; Sabolsky, E. M. Fabrication and Testing of High-Temperature Nano-Derived Resistive-Type Microsensors for Hydrogen Sensing. *J. Electrochem. Soc.* **2014**, *161*, B3094-3102.

(34) Ritala, M.; Niinistö, J. Atomic Layer Deposition. In *Chemical Vapor Deposition: Precursors, Processes and Applications*; Jones, A. C., Hitchman, M. L., Eds.; Royal Society of Chemistry: Cambridge, 2009; pp 158–206.

(35) George, S. M. Atomic Layer Deposition: An Overview. *Chem. Rev.* **2010**, *110*, 111–131.

(36) Ritala, M.; Leskelä, M. Atomic Layer Deposition. In *Handbook of Thin Film Materials*; Nalwa, H. S., Ed.; Academic: San Diego, 2002; Vol. 1, pp 103–159.

(37) Diskus, M.; Nilsen, O.; Fjellvåg, H. Growth of Thin Films of Molybdenum Oxide by Atomic Layer Deposition. *J. Mater. Chem.* **2011**, *21*, 705.

(38) Malm, J.; Sajavaara, T.; Karppinen, M. Atomic Layer Deposition of WO_3 Thin Films Using $W(CO)_6$ and O_3 Precursors. *Chem. Vap. Depos.* **2012**, *18*, 245–248.

(39) Song, J.-G.; Ryu, G. H.; Lee, S. J.; Sim, S.; Lee, C. W.; Choi, T.; Jung, H.; Kim, Y.; Lee, Z.; Myoung, J.-M.; Dusarrat, C.; Lansalot-Matras, C.; Park, J.; Choi, H.; Kim, H. Controllable Synthesis of Molybdenum Tungsten Disulfide Alloy for Vertically Composition-Controlled Multilayer. *Nat. Commun.* **2015**, *6*, 7817.

(40) Vos, M. F. J.; Macco, B.; Thissen, N. F. W.; Bol, A. A.; Kessels, W. M. M. Atomic Layer Deposition of Molybdenum Oxide from $(N^tBu)_2(NMe_2)_2Mo$ and O_2 Plasma. *J. Vac. Sci. Technol. A* **2016**, *34*, 01A103.

(41) Bertuch, A.; Sundaram, G.; Saly, M.; Moser, D.; Kanjolia, R. Atomic Layer Deposition of Molybdenum Oxide Using Bis(tert-Butylimido)bis(dimethylamido) Molybdenum. *J. Vac. Sci. Technol. A* **2014**, *32*, 01A119.

(42) Balasubramanyam, S.; Sharma, A.; Vandalon, V.; Knoops, H. C. M.; Kessels, W. M. M.; Bol, A. A. Plasma-Enhanced Atomic Layer Deposition of Tungsten Oxide Thin Films Using $(^tBuN)_2(Me_2N)_2W$ and O_2 Plasma. *J. Vac. Sci. Technol. A* **2018**, *36*, 01B103.

(43) Bergum, K.; Magrasó, A.; Fjellvåg, H.; Nilsen, O. Thin Film Fabrication and Characterization of Proton Conducting Lanthanum Tungstate. *J. Mater. Chem. A* **2014**, *2*, 18463–18471.

(44) Mouat, A. R.; Mane, A. U.; Elam, J. W.; Delferro, M.; Marks, T. J.; Stair, P. C. Volatile Hexavalent Oxo-Amidinate Complexes: Molybdenum and Tungsten Precursors for Atomic Layer Deposition. *Chem. Mater.* **2016**, *28*, 1907–1919.

(45) Jurca, T.; Peters, A. W.; Mouat, A. R.; Farha, O. K.; Hupp, J. T.; Lohr, T. L.; Delferro, M.; Marks, T. J. Second-Generation Hexavalent Molybdenum Oxo-Amidinate Precursors for Atomic Layer Deposition. *Dalt. Trans.* **2017**, *46*, 1172–1178.

(46) Nanayakkara, C. E.; Vega, A.; Liu, G.; Dezelah, C. L.; Kanjolia, R. K.; Chabal, Y. J. Role of Initial Precursor Chemisorption on Incubation Delay for Molybdenum Oxide Atomic Layer Deposition. *Chem. Mater.* **2016**, *28*, 8591–8597.

(47) Drake, T. L.; Stair, P. C. Vapor Deposition of Molybdenum Oxide Using Bis(ethylbenzene) Molybdenum and Water. *J. Vac. Sci. Technol. A* **2016**, *34*, 051403.

(48) Mattinen, M.; King, P. J.; Khriachtchev, L.; Heikkilä, M. J.; Fleming, B.; Rushworth, S.; Mizohata, K.; Meinander, K.; Räisänen, J.; Ritala, M.; Leskelä, M. Atomic Layer Deposition of Crystalline Molybdenum Oxide Thin Films and Phase Control by Post-Deposition Annealing. *Mater. Today Chem.* **2018**, *9*, 17–27.

(49) Moody, M. J.; Henning, A.; Jurca, T.; Shang, J. Y.; Bergeron, H.; Balla, I.; Olding, J. N.; Weiss, E. A.; Hersam, M. C.; Lohr, T. L.; Marks, T. J.; Lauhon, L. J. Atomic Layer Deposition of Molybdenum Oxides with Tunable Stoichiometry Enables Controllable Doping of MoS_2. *Chem. Mater.* **2018**, *30*, 3628–3632.

(50) Song, J.-G..; Park, J.; Lee, W.; Choi, T.; Jung, H.; Lee, C. W.; Hwang, S.-H; Myoung, J. M.; Jung, J.-H.; Kim, S.-H.; Lansalot-Matras, C.; Kim, H. Layer-Controlled, Wafer-Scale and Conformal Synthesis of Tungsten Disulfide Nanosheets Using Atomic Layer Deposition. *ACS Nano* **2013**, *7*, 11333–11340.

(51) Tägtström, P.; Mårtensson, P.; Jansson, U.; Carlsson, J.-O. Atomic Layer Epitaxy of Tungsten Oxide Films Using Oxyfluorides as Metal Precursors. *J. Electrochem. Soc.* **1999**, *146*, 3139–3143.

(52) Dezelah, C. L.; El-Kadri, O. M.; Szilágyi, I. M.; Campbell, J. M.; Arstila, K.; Niinistö, L.; Winter, C. H. Atomic Layer Deposition of Tungsten(III) Oxide Thin Films from $W_2(NMe_2)_6$ and Water: Precursor-Based Control of Oxidation State in the Thin Film Material. *J. Am. Chem. Soc.* **2006**, *128*, 9638–9639.

(53) Strobel, A.; Schnabel, H.-D.; Reinhold, U.; Rauer, S.; Neidhardt, A. Room Temperature Plasma Enhanced Atomic Layer Deposition for TiO_2 and WO_3 Films. *J. Vac. Sci. Technol. A* **2016**, *34*, 01A118.

(54) Cwik, S.; Milanov, A. P.; Gwildies, V.; Thiede, T. B.; Vidyarthi, V. S.; Savan, A.; Meyer, R.; Becker, H.-W.; Rogalla, D.; Ludwig, A.; Fischer, R. A.; Devi, A. Engineered Tungsten Oxy-Nitride Thin Film Materials for Photocatalytical Water Splitting Fabricated by MOCVD. *ECS Trans.* **2010**, *28* (8), 159–165.

(55) de los Arcos, T.; Cwik, S.; Milanov, A. P.; Gwildies, V.; Parala, H.; Wagner, T.; Birkner, A.; Rogalla, D.; Becker, H.-W.; Winter, J.; Ludwig, A.; Fischer, R. A.; Devi, A. Influence of Process Parameters on the Crystallinity, Morphology and Composition of Tungsten Oxide-Based Thin Films Grown by Metalorganic Chemical Vapor Deposition. *Thin Solid Films* **2012**, *522*, 11–16.

(56) Srinivasan, N. B.; Thiede, T. B.; de los Arcos, T.; Gwildies, V.; Krasnopolski, M.; Becker, H.-W.; Rogalla, D.; Devi, A.; Fischer, R. A. Transition Metal Nitride Thin Films Grown by MOCVD Using Amidinato Based Complexes $[M(N^tBu)_2\{(^iPrN)_2CMe\}_2]$ (M = Mo, W) as Precursors. *Surf. Coat. Technol.* **2013**, *230*, 130–136.

(57) Cwik, S.; Mitoraj, D.; Reyes, O. M.; Rogalla, D.; Peeters, D.; Kim, J.; Schütz, H. M.; Bock, C.; Beranek, R.; Devi, A. Direct Growth of MoS_2 and WS_2 Layers by Metal Organic Chemical Vapor Deposition. *Adv. Mater. Interfaces* **2018**, *5*, 1800140.

(58) Suntola, T. Atomic Layer Epitaxy. *Thin Solid Films* **1992**, *216*, 84–89.

(59) Gwildies, V.; Thiede, T. B.; Amirjalayer, S.; Alsamman, L.; Devi, A.; Fischer, R. A. All-Nitrogen Coordinated Amidinato/imido Complexes of Molybdenum and Tungsten: Syntheses and Characterization. *Inorg. Chem.* **2010**, *49*, 8487–8494.

(60) Waldo, R. A. An Iteration Procedure to Calculate Film Compositions and Thicknesses in Electron-Probe Microanalysis. In *Microbeam Analysis*; Newbury, D. E., Ed.; San Francisco Press: San Francisco, 1988; pp 310–314.

(61) CRC Handbook of Chemistry and Physics, 98th ed. [Online]; CRC Press: Boca Raton, FL, 2017–2018; http://hbcpnetbase.com (accessed May 3, 2018)

(62) Niskanen, A.; Hatanpää, T.; Ritala, M.; Leskelä, M. Thermogravimetric Study of Volatile Precursors for Chemical Thin Film Deposition. Estimation of Vapor Pressures and Source Temperatures. *J. Therm. Anal. Calorim.* **2001**, *64*, 955–964.

(63) Puurunen, R. L. Surface Chemistry of Atomic Layer Deposition: A Case Study for the Trimethylaluminum/Water Process. *J. Appl. Phys.* **2005**, *97*, 121301.

(64) Szekeres, A.; Ivanova, T.; Gesheva, K. Spectroscopic Ellipsometry Study of CVD Molybdenum Oxide Films: Effect of Temperature. *J. Solid State Electrochem.* **2002**, *7*, 17–20.

(65) Deb, S. K. Physical Properties of a Transition Metal Oxide: Optical and Photoelectric Properties of Single Crystal and Thin Film Molybdenum Trioxide. *Proc. R. Soc. London Ser. A* **1968**, *304*, 211–231.

(66) Bilousov, O. V.; Ren, Y.; Törndahl, T.; Donzel-Gargand, O.; Ericson, T.; Platzer-Björkman, C.; Edoff, M.; Hägglund, C.

Atomic Layer Deposition of Cubic and Orthorhombic Phase Tin Monosulfide. *Chem. Mater.* **2017**, *29*, 2969–2978.

(67) Heil, S. B. S.; Langereis, E.; Roozeboom, F.; van de Sanden, M. C. M.; Kessels, W. M. M. Low-Temperature Deposition of TiN by Plasma-Assisted Atomic Layer Deposition. *J. Electrochem. Soc.* **2006**, *153*, G956–965.

(68) Howard, C. J.; Luca, V.; Knight, K. S. High-Temperature Phase Transitions in Tungsten Trioxide - the Last Word? *J. Phys:. Condens. Matter* **2002**, *14*, 377–387.

(69) Nishide, T.; Mizukami, F. Control of Refractive Index of Sol-Gel Tungsten Oxide Films. *J. Sol-Gel Sci. Technol.* **1996**, *6*, 263–267.

(70) Sawada, S.; Danielson, G. C. Optical Indices of Refraction of WO_3. *Phys. Rev.* **1959**, *113*, 1008–1013.

(71) Quincy, R. B.; Houalla, M.; Proctor, A.; Hercules, D. M. Distribution of Molybdenum Oxidation States in Reduced Mo/TiO_2 Catalysts: Correlation with Benzene Hydrogenation Activity. *J. Phys. Chem.* **1990**, *94*, 1520–1526.

(72) Baltrusaitis, J.; Mendoza-Sanchez, B.; Fernandez, V.; Veenstra, R.; Dukstiene, N.; Roberts, A.; Fairley, N. Generalized Molybdenum Oxide Surface Chemical State XPS Determination via Informed Amorphous Sample Model. *Appl. Surf. Sci.* **2015**, *326*, 151–161.

(73) Irfan; Ding, H.; Gao, Y.; Small, C.; Kim, D. Y.; Subbiah, J.; So, F. Energy Level Evolution of Air and Oxygen Exposed Molybdenum Trioxide Films. *Appl. Phys. Lett.* **2010**, *96*, 243307.

(74) Vasilopoulou, M.; Douvas, A. M.; Georgiadou, D. G.; Palilis, L. C.; Kennou, S.; Sygellou, L.; Soultati, A.; Kostis, I.; Papadimitropoulos, G.; Davazoglou, D.; Argitis, P. The Influence of Hydrogenation and Oxygen Vacancies on Molybdenum Oxides Work Function and Gap States for Application in Organic Optoelectronics. *J. Am. Chem. Soc.* **2012**, *134*, 16178–16187.

(75) Greiner, M. T.; Chai, L.; Helander, M. G.; Tang, W.-M.; Lu, Z.-H. Transition Metal Oxide Work Functions: The Influence of Cation Oxidation State and Oxygen Vacancies. *Adv. Funct. Mater.* **2012**, *22*, 4557–4568.

(76) Miyata, N.; Akiyoshi, S. Preparation and Electrochromic Properties of RF-Sputtered Molybdenum Oxide Films. *J. Appl. Phys.* **1985**, *58*, 1651–1655.

(77) Carcia, P. F.; McCarron, E. M. Synthesis and Properties of Thin Film Polymorphs of Molybdenum Trioxide. *Thin Solid Films* **1987**, *155*, 53–63.

(78) Sabolsky, E. M.; Çiftyürek, E.; Wildire, C.; Sabolsky, K.; Taub, J.; Sierros, K.; Evans, T. H. Nano-Derived Microsensors for Monitoring Gas Species in Harsh-Environments. *ECS Trans.* **2014**, *61*, 375–385.

Table of Contents Graphic